Atmospheric
Chemistry
and Physics

Effect of chemically induced fracturing on the ice nucleation activity of alkali feldspar

Alexei A. Kiselev[1], **Alice Keinert**[1], **Tilia Gaedeke**[1], **Thomas Leisner**[1,2], **Christoph Sutter**[3], **Elena Petrishcheva**[3], **and Rainer Abart**[3]

[1]Karlsruhe Institute of Technology, Institute of Meteorology and Climate Research, Karlsruhe, Germany
[2]Institut für Umweltphysik, Universität Heidelberg, Heidelberg, Germany
[3]Department of Lithospheric Research, University of Vienna, Althanstrasse 14, 1090 Vienna, Austria

Correspondence: Alexei A. Kiselev (alexei.kiselev@kit.edu)

Abstract. Feldspar is an important constituent of airborne mineral dust. Some alkali feldspars exhibit particularly high ice nucleation (IN) activity. This has been related to structural similarities of the ice $(10\bar{1}0)$ prism planes and the (100) planes of alkali feldspar. Here the effect of generating feldspar surfaces with close to (100) orientation by means of chemically induced fracturing on the IN activity of alkali feldspar was investigated experimentally. To this end, gem-quality K-rich alkali feldspar was shifted towards more Na-rich compositions by cation exchange with an NaCl–KCl salt melt at 850 °C. By this procedure, a system of parallel cracks with an orientation close to the (100) plane of the feldspar was induced. Droplet-freezing assay experiments performed on grain mounts of the cation-exchanged alkali feldspars revealed an increase in the overall density of ice-nucleating active site (INAS) density with respect to the untreated feldspar. In addition, annealing at 550 °C subsequent to primary cation exchange further enhanced the INAS density and led to IN activity at exceptionally high temperatures. Although very efficient in experiment, fracturing by cation exchange with an alkali halide salt is unlikely to be of relevance in the conditioning of alkali feldspars in nature. However, parting planes with similar orientation as the chemically induced cracks may be generated in lamellar microstructures resulting from the exsolution of initially homogeneous alkali feldspar, a widespread phenomenon in natural alkali feldspar known as perthite formation. Perthitic alkali feldspars indeed show the highest IN activity. We tentatively ascribe this phenomenon to the preferential exposure of feldspar crystal surfaces oriented sub-parallel to (100).

1 Introduction – mineralogical aspects and relevance for atmospheric science

Feldspar is the most abundant mineral in the Earth's crust. It is a major constituent of magmatic, metamorphic, and sedimentary rocks (Smith and Brown, 1988), and due to its ubiquity on the Earth's surface, feldspar is also an abundant constituent of the solid aerosol particles. Desert dust (Boucher et al., 2014) and volcanic ash (Durant et al., 2008, 2010) are the main sources of airborne mineral dust contributing about 1000–4000 and 176–256 Tg/a, respectively. Solid aerosol particles are of interest in the context of ice formation in clouds. Mineral dust may substantially increase the freezing temperature of supercooled cloud droplets and foster the formation of ice particles at relatively high temperatures (Tang et al., 2016). Atmospheric ice particles have a strong influence on the physical properties of clouds and exert first-order controls on processes such as radiative transfer, precipitation, and absorption of trace gases (Kanji et al., 2017). Moreover, the albedo of clouds generally increases with the formation of ice particles (McFarquhar et al., 2002), an effect that is of pivotal importance for the Earth's radiation budget and is thus a key factor for global climate (Boucher et al., 2014; Bony et al., 2006). Among the different types of airborne mineral dust particles, some feldspars have been reported to have particularly high ice nucleation (IN) activity (Atkinson et al., 2013; Harrison et al., 2016; Peckhaus et al., 2016).

Feldspar is a framework silicate and forms a ternary solid solution among the Ca ($Ca_2Al_2Si_2O_8$ – anorthite), Na ($NaAlSi_3O_8$ – albite), and K ($KAlSi_3O_8$ – potassium feldspar) end-members, where the last two pertain to the alkali feldspar solid solution. The crystal structure of feldspar is comprised of a three-dimensional framework of corner-sharing SiO_4 and AlO_4 tetrahedrons with the alkali and alkali earth cations located in large framework cavities. Depending on chemical composition, pressure, temperature, and the state of Al–Si ordering on the tetrahedral sublattice, feldspar may have monoclinic $C2/m$ or triclinic $C\bar{1}$ symmetry (Ribbe, 1983). The mineralogy of feldspar has a crucial effect on its ability to cause freezing of supercooled water. The ice-nucleating efficacy expressed in terms of the ice-nucleating active site (INAS) surface density ($n_s(T)$; Connolly et al., 2009) was shown to vary over 2 orders of magnitude for various alkali feldspars (Harrison et al., 2016). Perthites, which are exsolved feldspars that typically take the form of (sub)micron-scale lamellar intergrowth of more K-rich and more Na-rich alkali feldspar, were found to have the highest IN efficacy among all feldspar dust particles (Whale et al., 2017). The mechanisms relating the lamellar microstructure formed by exsolution and enhanced IN efficacy are, however, not known and are currently debated.

In a previous study that used natural perthitic alkali feldspars, the preferential epitaxial nucleation and growth of ice crystals by the alignment of the ice $(10\bar{1}0)$ prism plane with (100) faces of the feldspar was identified as the key mechanism underlying the high IN activity of alkali feldspar in deposition freezing (Kiselev et al., 2017). The proposed mechanism was supported by a later study by Pach and Verdaguer (2019) but could not be reproduced by molecular dynamic (MD) simulation (Soni and Patey, 2019). In this latter study it was suggested that the (100) surfaces need to be structurally rearranged or chemically altered to enable the preferential oriented nucleation of ice crystals.

Facets with (100) orientation do, however, not pertain to the commonly exposed crystal surfaces of alkali feldspar. The surfaces of natural feldspar are either represented by the typical growth facets including the (110), $(\bar{1}01)$, (001), $(20\bar{1})$, and (010) facets (Smith and Brown, 1988) or by the (001) and (010) cleavage planes where the cleavage is perfect on the (001) plane and good on the (010) plane. Crystal surfaces with (100) orientation have high surface energy, and (100) facets or cleavage planes hardly ever occur. It has been argued that small patches of (100) crystal surfaces may be exposed at defects such as cracks and cavities (Kiselev et al., 2017). Holden et al. (2019) observed nucleation of ice in supercooled water in contact with feldspar, where the ice nucleation appeared to be associated with pits on the specimen surface. In this context perthites are of particular interest. The boundaries between the more Na-rich and the more K-rich lamellae of perthite are oriented so that the crystallographic lattice misfit between the compositionally distinct lamellae is minimized. This condition defines the so-called

Murchison plane (Fitz Gerald et al., 2006; Smith and Brown, 1988), which has non-rational Miller indices between $(\bar{6}01)$ and $(\bar{8}01)$. The Murchison plane does, in general, not coincide with any of the primary atomic planes. It is oriented sub-parallel to (100) within 8 to 11°, and parting planes following the Murchison plane may well contain patches of (100) crystal surface (see Fig. S4 in the Supplement for the orientation of chemically induced cracks and of the Murchison plane relative to (100)). In light of the extraordinarily high IN activity of alkali feldspar and the preferential epitaxial nucleation of ice on feldspar (100) surfaces, it is important to understand the mechanisms by which such surfaces may form and to what extent the IN activity of these surfaces differs from the IN activity of the more commonly exposed growth facets and cleavage planes of alkali feldspar. In particular, the potential effects of different formation mechanisms and associated crystal surface morphologies on the efficacy of IN on alkali feldspar aerosol particles is of interest. In this communication we investigate the IN activities of alkali feldspars that were subject to different pretreatments designed to mimic natural processes leading to the exposure of crystal surfaces sub-parallel to (100). We relate the IN activity to the mode and the extent of the modification of the crystal surface by fracturing and discuss the potential role that (100) surfaces play for the IN activity of alkali feldspars.

2 Experiment

2.1 Sample preparation

2.1.1 Cation exchange and annealing experiments

For preparing feldspar fragments with a significant fraction of (100) surfaces, we made use of the fact that fracturing of alkali feldspar sub-parallel to the Murchison plane may be induced by shifting the composition of a K-rich alkali feldspar towards more Na-rich compositions by diffusion-mediated Na–K cation exchange with an NaCl–KCl salt melt (Neusser et al., 2012; Petrishcheva et al., 2019; Predan et al., 2020; Scheidl et al., 2014). This effect is due to the strongly anisotropic contraction of the crystal structure with increasing Na content (Kroll et al., 1986; Angel et al., 2012) with the strongest contraction approximately perpendicular to the Murchison plane. During diffusion-mediated cation exchange with NaCl–KCl salt melt of appropriate composition, a more Na-rich layer forms on the surface of the specimen, while the original more K-rich composition is retained in the internal regions. Both the internal regions with zero compositional eigenstrain state and the more Na-rich surface layer with strong negative eigenstrain state perpendicular to the Murchison plane pertain to one solid, and a tensile stress state is induced in the chemically altered surface layer. When the compositional shift towards more Na-rich compositions of the surface layer exceeds a certain extent, a critical stress
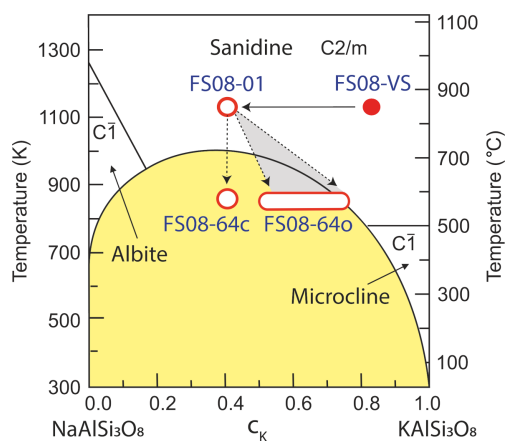
Figure 1. Schematic isobaric phase diagram for alkali feldspar showing the stability fields and respective symmetries of albite, sanidine, and microcline; the miscibility gap (the shaded yellow region under the solvus curve) represents the two-phase region; the filled red circle shows the original composition of the Volkesfeld sanidine (sample FS08-VS), which was shifted to intermediate composition by cation exchange at 850 °C (sample FS08-01); subsequent annealing at 550 °C in vacuum produced sample FS08-64c, and annealing at 550 °C in contact with the NaCl–KCl salt produced sample FS08-64o with a somewhat variable composition due to incomplete cation exchange (see below).

level is reached, followed by fracturing approximately parallel to the Murchison plane that is perpendicular to the direction of strongest contraction of the crystal structure (Neusser et al., 2012; Petrishcheva et al., 2019; Scheidl et al., 2014; Predan et al., 2020).

We exploited this mechanical effect for producing surfaces with orientations close to (100) by performing cation exchange experiments using powders of gem-quality alkali feldspar and an NaCl–KCl salt mixture as starting materials. The original feldspar is a sanidine from Volkesfeld (Eifel, Germany) with $c_K^{fsp} = 0.84$, where c_K^{fsp} is the atomic site fraction of K on the alkali sublattice; $c_K^{fsp} = [K]/([Na] + [K])$ (marked with the solid red circle in the phase diagram in the Fig. 1). The feldspar was gently crushed and sieved, and the grains of the 100–200 μm sieve fraction were exchanged with a mixed molten NaCl–KCl salt with a composition of $c_K^{salt} = 0.21$ at 850 °C for 8 d to attain equilibrium Na/K partitioning between feldspar and the salt. The salt was applied in excess so that it practically retained its composition unchanged during the cation exchange experiment. At 850 °C the composition of Volkesfeld sanidine in equilibrium with NaCl–KCl salt melt with $c_K^{salt} = 0.21$ is $c_K^{fsp} = 0.43$ (Neusser et al., 2012). The induced compositional change corresponds to a shift of $\Delta c = 0.41$ towards more Na-rich compositions.

At 850 °C Na–K exchange equilibrium between the surface of alkali feldspar and an NaCl–KCl salt melt is closely approached within less than a day (Schäffer et al., 2014b). With time, the chemically altered surface layer grows in

thickness. This process is controlled by the interdiffusion of Na and K on the alkali sublattice of the feldspar. According to the calibration of Na–K interdiffusion in alkali feldspar by Schäffer et al. (2014a) and by Petrishcheva et al. (2014, 2020) in 8 d at 850 °C, the diffusion front would propagate a distance of 20 to 30 μm, depending on crystallographic direction. The compositional shift in the chemically altered surface layer produced sufficiently large tensile stress so that fracturing was induced, and a system of parallel cracks with an orientation close to the Murchison plane developed (see further down).

After the cation exchange, the feldspar samples were split into three batches. One batch was annealed at 550 °C for 64 d, while the grains were kept in contact with the salt so that further cation exchange between the salt and the feldspar occurred. At 550 °C the salt is solidified and cation exchange is slower than during the primary cation exchange, but it is still sufficiently fast so that the resulting chemical alteration can well be detected (see below). We refer to this annealing route as the *open system setting*, and the sample produced by this route is labeled FS08-64o. A second batch of cation-exchanged feldspar grains was removed from the salt and annealed at 550 °C in vacuum for 64 d. The conditions lay within the miscibility gap of alkali feldspar (the shaded yellow region in Fig. 1), which is a region on the isobaric phase diagram where two alkali feldspars of different composition coexist in equilibrium (Work et al., 2004; Brown and Parsons, 1984). At these conditions, phase separation of the originally compositionally homogeneous feldspar with $c_K^{fsp} = 0.43$ into submicron-scale lamellas of more K-rich and more Na-rich feldspars may have occurred (Petrishcheva et al., 2020) but was not observed in this study, as this would have required targeted analysis by transmission electron microscopy, which was beyond our scope. We refer to this annealing route as the *closed system setting*, and the sample produced is labeled FS08-64c. A third batch of cation-exchanged feldspar grains was removed from the melt after the primary cation exchange. It was rinsed with distilled water to remove the salt and then gently dried and stored without further treatment. This sample is labeled FS08-01. The details of the treatment are illustrated in Fig. 1, and the properties of the resulting feldspar grains are summarized in Table 1. Grain mounts were prepared from all three sample batches as described in the next section.

2.1.2 Preparation of grain mounts and thin sections

The amount of chemically altered feldspar prepared as described in the previous section was too small for conducting droplet-freezing experiments with aqueous suspensions of feldspar powder, as usually done in mineral dust IN efficiency studies, as in Hiranuma et al. (2015). As an alternative, we prepared grain mounts by casting feldspar grains in a thin layer of epoxy resin on top of a standard microscope glass slide. After solidification of the resin, the layer

Table 1. Overview of the feldspar samples and experimental conditions. NA stands for "not applicable".

Sample label	Sample origin and preparation	Preparation for cold-stage experiments	Number of droplets	Droplet footprint area, S_d [m^2]	Contact area of feldspar–droplet interface [m^2]
FS08-VS	Sanidine from Volkesfeld, Eifel, Germany; ground and sieved to $< 20\,\mu m$	Aqueous particle suspension 0.1 wt % 1 wt %	160	2.1×10^{-7}	$(3.9 \pm 0.4) \times 10^{-9}$ $(3.9 \pm 0.4) \times 10^{-8}$
FS08-Epx	Feldspar-free epoxy resin	Grain-free epoxy resin mount, ground and polished $< 1\,\mu m$, ion milled	540	1.2×10^{-8}	NA
FS08-01	Albite-shifted sanidine, 8 d at 850 °C in NaCl–KCl salt mixture melt	Grain mount, ground and polished $< 1\,\mu m$, ion milled	386	9.9×10^{-9}	$(12.9 \pm 1.5) \times 10^{-10}$
FS08-64o	Albite-shifted sanidine tempered at 550 °C for 64 d in NaCl–KCl salt mixture melt	Grain mount, ground and polished $< 1\,\mu m$, ion milled	504	1.2×10^{-8}	$(39.4 \pm 1.8) \times 10^{-10}$
FS08-64c	Albite-shifted sanidine tempered at 550 °C for 64 d in vacuum	Grain mount, ground and polished $< 1\,\mu m$, ion milled	523	7.8×10^{-9}	$(16.7 \pm 1.2) \times 10^{-10}$
FS06-010	Pakistan feldspar (41 % or., 39 % mic., 20 % ab.), showing polysynthetic twinning according to the pericline law and K–Na exsolution lamella structure	Thin section for optical microscopy ($\sim 20\,\mu m$), polished to $< 1\,\mu m$, ion milled	340	1.9×10^{-8}	1.9×10^{-8}

of cast epoxy–feldspar aggregate was ground to a thickness of 200 μm and subsequently polished to optical quality. Through this procedure, the majority of the feldspar grains were exposed on the polished sample surface. The grain mounts were cut into 10 mm × 10 mm square plates and end-polished using a Leica TIC3X ion-milling device. A current of 0.5 mA and an acceleration voltage of 1 kV were applied for 45 min, and the sample was continuously rotated in the horizontal plane. The same procedure was applied for preparing grain-free mounts of epoxy resin (FS08-Epx) to be used for reference measurements.

The grain mounts were analyzed by polarization microscopy using a Leica DM4 polarization microscope and in a FEI Thermo Fisher Quattro environmental scanning electron microscope (ESEM) equipped with an EDAX Octane Super energy dispersive X-ray spectrometer (EDS). Exemplary views of the grain mount prepared from the cation-exchanged alkali feldspar (sample FS08-01) are shown in Fig. 2. For comparison, a natural perthitic alkali feldspar from Pakistan (sample FS06-010) was analyzed. The sample was prepared from a centimeter-sized specimen with partially developed facets. Visually, the feldspar specimen is pale beige and turbid (see Fig. S1). The X-ray diffraction (XRD, Panalytical, Cu Kα 1 and 2) analysis yielded a phase content of 41 % orthoclase, 39 % microcline, and 20 % albite (see Supplement for details).

In transmitted light optical microscopy and in the SEM, a complex microperthitic structure overlain by polysynthetic twinning after the pericline law and porosity, which is very likely related to hydrothermal or deuteric alteration, were identified (see Fig. S2). For our experiments, the specimen was cut parallel to the (010) cleavage plane, and a thin section was prepared employing the same polishing routine as used for the grain mounts. The crystallographic orientation of the cleavage plane was confirmed by backscattered electron diffraction (BSED) obtained with a Hikari Super BSED detector (EDAX AMETEK) mounted on the ESEM. The BSED patterns were analyzed with the EDAX OIM v8.0 software package using the built-in structure file of generic triclinic feldspar. The thin sections with different orientations pre-
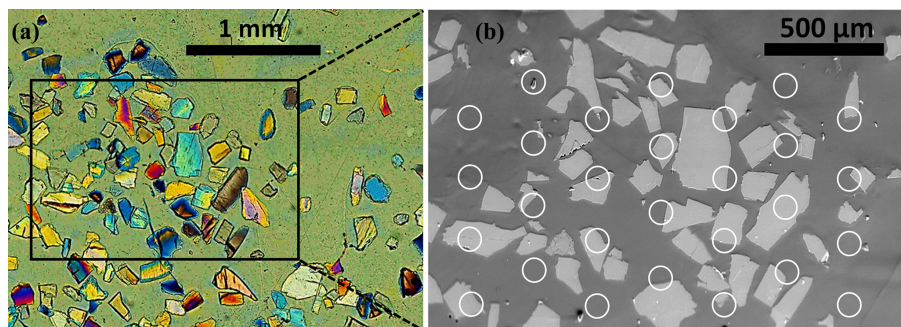
Figure 2. Grain mounts used in the droplet-freezing assay study. **(a)** Optical microscope image in transmitted light with crossed-polarizers and first-order retardation plate showing feldspar grains embedded in epoxy resin (sample FS08-01). **(b)** Backscattered electron (BSE) image of the area marked by the black frame in **(a)**. The white circles illustrate the footprints of water droplets used in the cold-stage experiment.

pared from the same specimen have been reserved for a different study which is currently under evaluation.

2.2 Droplet-freezing assay experiments: measurement routine and calculation of INAS density

The ice-nucleating efficacy of the altered feldspar was measured in the droplet-freezing assay setup previously described in Peckhaus et al. (2016). Briefly, a 10 mm by 10 mm grain mount was placed into a temperature-controlled cold-stage setup consisting of a Linkam MDBCS-196 motorized cold stage, a piezo-driven drop-on-demand dispenser (GeSIM, model A010-006 SPIP), and a video camera with a wide-field objective allowing for detection of individual freezing events with 0.125 s time resolution. In the experiments described in this work, nearly 500 droplets of pure water each with a volume of approximately 0.4 nL were deposited onto the polished surface of the grain mount in a checkerboard pattern with 400 μm center-to-center separation distance between the droplets (see Fig. 2b). During the freezing experiments, the cold stage was cooled with a rate of 3 K/min. The temperature was monitored with a thin-film platinum resistance sensor (Pt-100) that was fixed directly on the sample surface using a vacuum-grade heat-conducting paste. Freezing of individual droplets was detected by an intensity change of the light reflected by the droplets, which happens at the moment of freezing and is best detected using crossed polarizers. An automated LabView video analysis routine was used to identify the individual droplet positions and freezing temperatures and for calculating the fraction of frozen droplets as a function of temperature $f_{ice}(T)$ (see Fig. 5a). To account for the different freezing efficacies of feldspar and epoxy resin, several freezing experiments were conducted with the droplets deposited on the surface of a feldspar-free epoxy mount (sample FS08-Epx). For each sample, at least three replicate measurements were done. Between successive measurements the droplets were evaporated and redeposited in the similar pattern. Note, however, that, due to the limited positioning accuracy of the motorized

cooling stage, the new pattern could be shifted with respect to the previous one by a distance of up to 100 μm in random direction. During the cooling ramp, some droplets located near the side of the grain mount have reduced their sizes or disappeared completely due to evaporation. These droplets were excluded from the post-processing analysis, resulting in a fewer total number of droplets actually used for evaluation of the INAS density of feldspar (see Table 1 for the actual total number of droplets in every experiment). The droplet footprint area was obtained by measuring 20 randomly chosen droplet contours in a video frame recorded just before the detection of the first freezing event. In this way the gradual droplet evaporation and associated reduction of footprint area during the cooling ramp could be taken into account.

The heterogeneous freezing efficacy of a substrate is usually expressed in terms of the INAS density (Murray et al., 2012; Connolly et al., 2009). Within the framework of the classical nucleation theory (see Hoose and Möhler, 2012), the INAS density $n_s(T)$ at temperature T is obtained from the fraction of frozen droplets $f_{ice}(T)$ and the area of contact S_d between the droplet and the substrate:

$$n_s(T) = -\frac{\ln(1 - f_{ice}(T))}{S_d}. \tag{1}$$

The average water–feldspar contact area was determined from the droplet size and from the exposed surface area of the feldspar grains. Due to the comparable size of the footprints of the droplets and the feldspar fragments exposed on the sample surface, a droplet may be in contact with feldspar and epoxy resin or it may be in contact with epoxy resin exclusively (see Fig. 2b). This is why the IN efficacy of the epoxy resin needs to be considered. Moreover, in the replicate experiments the droplets were deposited on slightly different positions; therefore, the water–feldspar contact area did not only vary from droplet to droplet but also between replicate measurements. The water–feldspar contact area was evaluated using the backscattered electron microscope images of the grain mounts (Fig. 3). A black-and-white binary mask created from the segmented image of a grain map was over-

lain with the contour image of a droplet array, as illustrated in Fig. 3, and the average overlapping area S_{FS} per droplet was determined. Given that the number of IN active sites associated with the surface of feldspar grains $n_s^{FS}(T)$ and the number of INAS associated with the surface of epoxy resin $n_s^{EPX}(T)$ are additive, we may write

$$n_s^{app}(T) \cdot S_d = n_s^{FS}(T) \cdot S_{FS} + n_s^{EPX}(T) \cdot S_{EPX}, \quad (2)$$

where $n_s^{app}(T)$ is the apparent INAS density obtained from the droplet-freezing experiments via Eq. (1), and S_{FS} and S_{EPX} represent the average droplet–feldspar and droplet–epoxy contact areas, respectively, which satisfy the condition $S_d = S_{FS} + S_{EPX}$. Combining Eqs. (1) and (2), the INAS density associated with feldspar grains is calculated as

$$n_s^{FS}(T) = -\frac{\ln(1 - f_{ice}(T))}{S_{FS}} - n_s^{EPX}(T) \cdot \left(\frac{S_d}{S_{FS}} - 1\right), \quad (3)$$

with $n_s^{EPX}(T)$ obtained from the droplet-freezing experiments conducted on the grain-free mount of epoxy resin (sample FS08-Epx).

The actual position of every droplet could not be measured precisely as the resolution of the main camera was not sufficient to recognize the footprint of every droplet automatically. Therefore, the droplet array was created using the coordinates of the individual droplets identified by the video processing software and the diameter of droplet footprint measured manually for several droplets clearly visible in the video frames. To estimate the error arising from use of such *synthetic* droplet array, the calculation of S_{FS} was repeated 100 times for every grain mount with the position of every droplet in the array varying randomly within a droplet diameter from the initial position. The resulting distribution of S_{FS} values was used to obtain the mean feldspar–water overlapping area per droplet and its standard deviation, which was then used for calculating the INAS density. The values of S_{FS} and the corresponding standard deviations are given in the last column of Table 1. The standard deviations of S_{FS} were used to estimate the uncertainty of the INAS density, which was found to be within $\pm 100\%$ from the mean value for all measurements conducted with the grain mounts.

For reference, the original Volkesfeld sanidine (sample FS08-VS) was prepared as a powder by grinding the specimen in a mortar and sieving the powder through a 20 µm sieve. The powder was then used for preparing aqueous suspensions containing 0.1 wt % and 1 wt % feldspar. Suspension droplets with a volume of 21.6 nL were deposited in a 9×9 array with a PipeJet Nanodispenser (BioFluidix GmbH) on a clean 10 × 10 mm silicon wafer (Ted Pella, Inc.). About 10 droplets were deposited on top of the thin-film temperature sensor and could not be used for freezing measurements, so approximately 70 droplets in a single experiment could be used. Freezing of the suspension droplets was measured using the same device as described above; see also Peckhaus et al. (2016). For the calculation of the INAS density

of the sample FS08-VS, the specific surface area (SSA) of the feldspar powder was determined using an Autosorb iQ model 7 gas sorption system (Quantachrome Instruments, a brand of Anton Paar QuantaTec Inc.) Using Ar as a sorbent gas at 87 K and applying Brunauer–Emmett–Teller (BET) theory (Brunauer et al., 1938), the SSA of sample FS08-VS was found to be $(1.8 \pm 0.2)\,m^2/g$, implying a total surface area of the feldspar particles contained in a single droplet of $(3.9 \pm 0.4) \times 10^{-9}\,m^2$ for the 0.1 wt % suspension and of $(3.9 \pm 0.4) \times 10^{-8}\,m^2$ for the 1 wt % suspension.

For the droplet-freezing experiments on the thin section of Pakistan microcline (sample FS06-010), droplets with a volume of 1.4 nL were used. Accordingly, larger droplet footprint areas were taken into account when calculating the INAS density.

To estimate the possible effect of the purity of the water used in the experiments, we conducted several freezing experiments with pure water droplets deposited on a clean silicon wafer. The silicon wafer was shown previously to have no effect on ice nucleation (Peckhaus et al., 2016), and the freezing of droplets occurs within a narrow temperature interval between -35 and $-36\,°C$ as shown by the dashed curve in Fig. 4. When freezing occurs at temperature higher than this, the presence of an ice-nucleating substrate or of ice-nucleating particles suspended in a water droplet is inferred.

3   Results and discussion

3.1   Droplet-freezing experiments

The ability of feldspar to induce freezing of supercooled water was investigated in a series of droplet-freezing experiments as described in Sect. 2.2. The experimental results are summarized in Fig. 4. Panel (a) shows the fraction of frozen droplets as a function of supercooling temperature, and panel (b) shows the INAS density $n_s(T)$ calculated from the data presented in panel (a) and accounting for the contact area between supercooled water and feldspar (see Table 1). Representation of the results of the freezing experiments in terms of $n_s(T)$ allows for comparison of the IN efficacy of various substrates and powder samples even if obtained by different methods.

The droplet-freezing temperature is a function of substrate activity, droplet footprint area, and cooling rate; therefore, the freezing behavior of different samples cannot be directly compared based on the freezing curves alone (Fig. 4a). Nevertheless, some general features are clearly recognized. Freezing of more than 90 % of pure water droplets on a Si wafer occurs within a narrow temperature interval of 1 K. This behavior is characteristic for homogeneous freezing of supercooled water (see Ickes et al., 2015). The freezing curve of supercooled droplets on the epoxy resin (FS08-Epx) has a pronounced steep section between -28 and $-30\,°C$, where
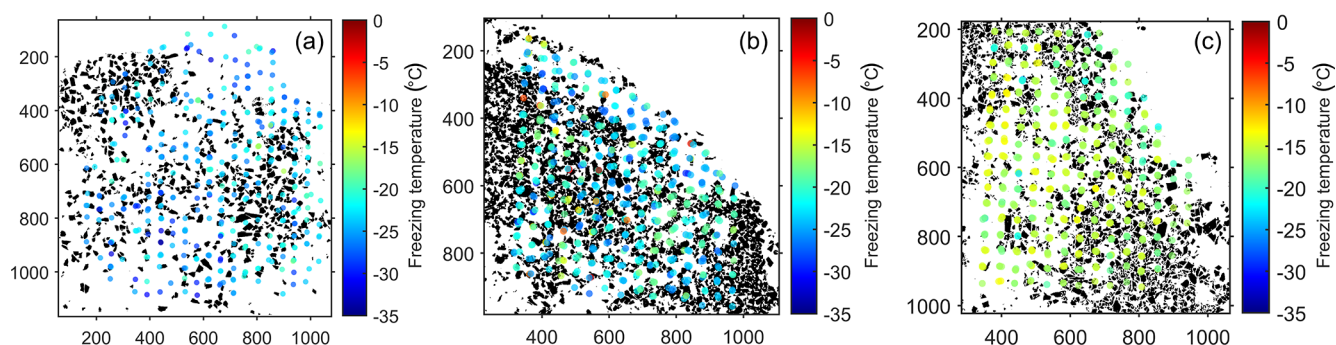
Figure 3. Binary images of grain mounts **(a)** FS08-01, **(b)** FS08-64o, and **(c)** FS08-64c, overlaid with the heat maps of droplet arrays color-coded according to the droplet-freezing temperatures. Heat maps for three repeated experiments are combined. The numbers on the *x* and *y* axes are pixel coordinates of the images. The pixel size is 8.8 μm.
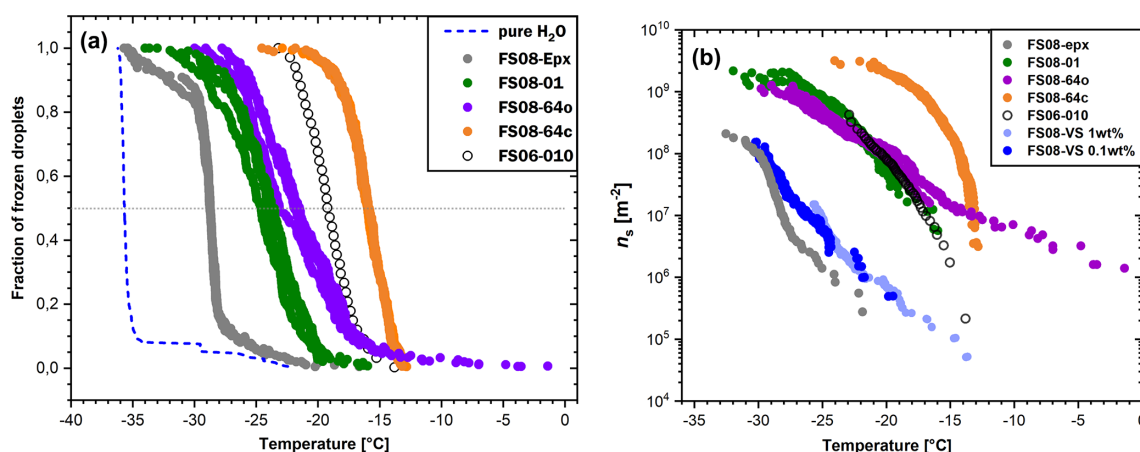
Figure 4. Results of the droplet-freezing experiments. **(a)** Fraction of frozen water droplets as a function of supercooling temperature. The cooling rate was 3 K/min in all experiments. Pure water droplets on a clean silicon wafer freeze within a small temperature range between -35 and $-36\,°C$ (as shown by the blue dashed curve). **(b)** INAS density calculated from the data shown in **(a)**. In addition, the INAS density calculated for the untreated Volkesfeld sanidine (sample FS08-VS) obtained from suspension droplet-freezing experiments is shown for comparison in two different shades of blue for the two weight concentrations (dark blue for 0.1 wt % and light blue for 1 wt %).

the majority of the droplets freeze almost simultaneously. This freezing behavior suggests that a single type of ice-nucleating active site, albeit with low freezing efficacy, prevails (Vali, 2008; Wright and Petters, 2013). The freezing curves of the samples containing feldspar exhibit less steep slopes, pointing to an intrinsic variability of ice-nucleating active sites in contact with a droplet of supercooled water.

Figure 4b shows the $n_s(T)$ curves obtained from the chemically altered feldspar and from the original Volkesfeld sanidine, together with the $n_s(T)$ curves for the epoxy resin and of the microcline from Pakistan (FS06-010). As expected, the epoxy resin has the lowest INAS density, followed by the original feldspar FS08-VS, the feldspar FS08-01 that was cation-exchanged at 850 °C, and the feldspars that were first cation-exchanged at 850 °C and then annealed at 550 °C in an open system setting (sample FS08-64o) and in a closed system setting (sample FS08-64c). Note that the original Volkesfeld sanidine was prepared as a powder, and

suspension droplets were used for the freezing experiments. Grinding of the material may introduce morphology changes beyond a general increase in the specific surface area (Hiranuma et al., 2014); the comparison of its IN activity with the IN activities of the other samples, which were determined from grain mounts, needs to be considered with caution. In spite of this uncertainty, it may be stated that the INAS density appears to increase substantially after the ion-exchange treatment. All ion-exchanged feldspars have substantially higher INAS densities than the untreated Volkesfeld sanidine. Recalling that Volkesfeld sanidine was used as the starting material for the cation exchange experiments, the observed difference in INAS density is ascribed to the effects of cation exchange. Apart from a shift in chemical composition, the most obvious effect of cation exchange is the generation of a system of parallel cracks that are oriented sub-parallel to the Murchison plane. The Murchison plane encloses an angle of about 8 to 11° with the (100) lattice plane, and, given that

the crack flanks are somewhat uneven, they probably contain patches of (100) crystal surface. An increase in the INAS density due to exposure of (100) crystal surfaces is well in line with the findings of Kiselev et al. (2017), who observed preferential epitaxial nucleation and growth of ice crystals on (100) surfaces of alkali feldspar. It was shown by the latter authors that the atomic structures of the ($10\bar{1}0$) prism planes of ice and the (100) planes of alkali feldspar have striking similarities allowing for efficient epitaxial nucleation and growth of ice on (100) surfaces of alkali feldspar. It must be noted that the epitaxy-driven nucleation of ice on feldspar (100) surfaces could not be reproduced in the MD simulation study of Soni and Patey (2019). Interestingly, the $n_s(T)$ of the cation-exchanged feldspar FS08-01 is very similar to the INAS density of the (010) thin section of Pakistan feldspar (sample FS06-010). The comparison between the two feldspar types is perfectly justified as identical preparation and measurement routines were applied for both samples, with the only difference being that the FS08-01 sample contains randomly oriented feldspar grains, whereas in the FS06-010 sample only the crystal plane with (010) orientation is exposed.

The annealing of the cation-exchanged samples at 550 °C leads to a further increase in the INAS density. Both sample FS08-64o, which was annealed in contact with the salt – open system setting – and sample FS08-64c, which was annealed in vacuum – closed system setting – show higher INAS densities than sample FS08-01, which was prepared from cation-exchanged Volkesfeld sanidine without subsequent annealing. Samples FS08-64o and FS08-64c show quite different freezing behavior. Whereas sample FS08-64c has a steep temperature dependency and the highest $n_s(T)$ values of all samples, the $n_s(T)$ curve of sample FS08-64o is less steep and extends to comparatively high temperatures, indicating that a set of very active ice-nucleating sites is capable of triggering ice nucleation at temperatures as high as −3 °C. However, at temperature below −15 °C, the FS08-64o sample has the same INAS density as the FS08-01. Ice nucleation at similarly high temperatures was reported from sample FS04 studied in Peckhaus et al. (2016).

3.2 Grain morphology and chemical composition

The grain morphologies and chemical compositions were characterized by ESEM for all samples except FS06-010, which was additionally studied with powder XRD (see Table 1). ESEM images of the cation-exchanged sample FS08-01 and of the cation-exchanged and annealed samples FS08-64o and FS08-64c are shown in Figs. 5 and S3. The most evident feature of all samples is the presence of a system of parallel cracks. The cracks extend at high angles to the (010) and the (001) cleavage planes bounding the feldspar fragments. In the cation-exchanged feldspar (FS08-01), the cracks are, however, hardly visible, whereas they are up to 5 μm wide and well visible in the annealed feldspars. In the

grains of sample FS08-64o, K-rich zones have developed along the cracks. In the backscattered electron (BSE) image, the K-rich zones appear as light grey bands flanking the cracks on both sides (dashed arrows in Fig. 5b). The K-rich zones were formed by successive Na–K exchange between the feldspar and the salt during annealing at 550°. It is inferred from the observed K-rich layers along the crack flanks that at this temperature potassium partitions more strongly into the feldspar than during the primary cation exchange at 850 °C. This induced local inverted diffusion of K during annealing at 550 °C and locally reversed the compositional shift attained during the primary cation exchange at 850 °C. No such K-rich zones are visible in the BSE images of feldspar FS08-64c. This is due to the fact that this sample was separated from the salt after primary cation exchange and subsequently annealed in vacuum at 550 °C. The feldspar fragments of this sample show uniform BSE contrast and appear to be compositionally homogeneous. From recent work (Petrishcheva et al., 2020) it is known that during the annealing at 550 °C an alkali feldspar with $c_K = 0.41$ may experience phase separation by spinodal decomposition. At the applied experimental conditions and annealing time, the spinodal decomposition typically produces an alternation of more Na-rich and more K-rich lamellae with a characteristic lamellar spacing on the order of 30 nm (Petrishcheva et al., 2020), a microstructure that is referred to as cryptoperthite (Smith and Brown, 1988). The nanometer-scaled lamellar intergrowth cannot be resolved with BSE imaging in the SEM and a uniform grey shade is observed. It has been shown by Petrishcheva et al. (2020) using scanning transmission electron microscopy (STEM) that the lamellae are coherently intergrown so that lamella boundaries are free of misfit dislocations, and the lattice misfit between the more Na-rich and the more K-rich lamellae is compensated by elastic strain. In contrast, misfit dislocations are frequently observed at lamellar boundaries in natural perthites (Lee et al., 1995; Abart et al., 2009).

The general enhancement of the IN activity by the chemically induced cracks is corroborated by the presence of abundant parallel cracks in all cation-exchanged samples. With respect to the differences in the INAS density between the cation-exchanged sample FS08-01, and the cation-exchanged and subsequently annealed samples FS08-64c and FS08-64o, it may be speculated that the narrow cracks of sample FS08-01 were less accessible to water than the more open cracks of the annealed samples. The fact that the $n_s(T)$ curve of sample FS08-64c has quite similar shape as the $n_s(T)$ curve of sample FS08-01 and is only shifted to higher temperatures suggests that annealing of sample FS08-64c in vacuum only led to a further limited extension of the cracks but did not change their morphological characteristics. The cracks become deeper and longer, thus exposing larger surface that might contain patches with (100) orientation. Limited propagation of the cracks even without a chemical driving force seems feasible in light of residual stresses that
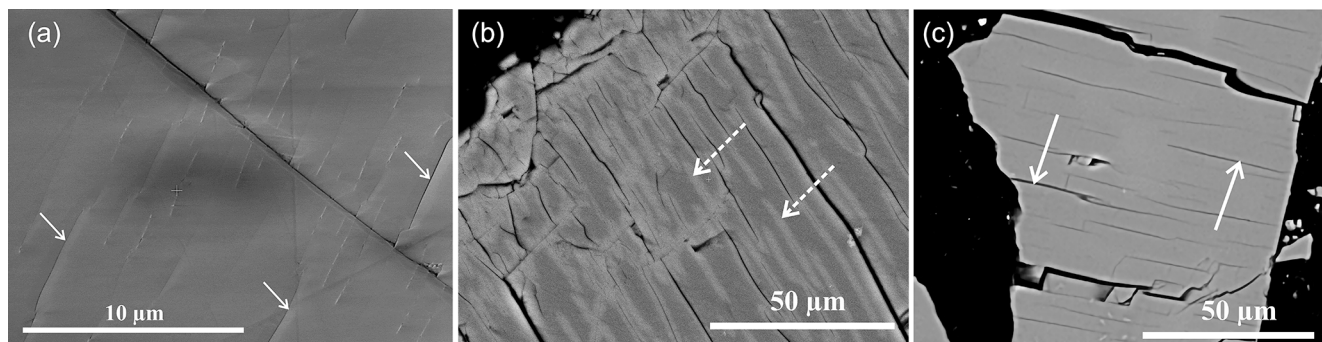
Figure 5. Backscattered electron (BSE) images of feldspar grains at different stages of the treatment. The arrows mark chemically induced cracks extending approximately parallel to the Murchison plane. **(a)** Surface of a sanidine grain after a compositional shift from $c_K = 0.84$ to $c_K = 0.43$ by cation exchange (cation-exchanged sample FS08-01). **(b)** Surface of a cation-exchanged sample after annealing at 550 °C for 64 d in contact with salt (open system setting, sample FS08-64o). The light grey bands (marked by the dashed arrows) are K-rich zones that are developed by reverse cation exchange along the cracks; dark areas correspond to the regions with higher concentration of Na. **(c)** Surface of cation-exchanged sample after annealing at 550 °C in vacuum for 64 d (closed system setting, sample FS08-64c). At the resolution of ESEM, this sample appears chemically homogeneous despite of the fact that the sample is exsolved forming a lamellar intergrowth with characteristic lamellar spacing of about 30 nm (Petrishcheva et al., 2020). The relatively straight grain edge on the right follows a (010) cleavage plane.

remained from the cation exchange experiment and newly induced thermal stresses. In contrast, the characteristics of the INAS was substantially modified during the annealing of sample FS08-64o in contact with salt.

It is known from earlier work (Neusser et al., 2012; Schäffer et al., 2014a) that lattice expansion associated with a compositional shift of Na-rich alkali feldspar towards more K-rich compositions may lead to the formation of cracks sub-parallel to the grain surface. The feldspar may then disintegrate by successively loosing material from a surface layer in an onion-skin fashion, a process referred to as "spalling". Formation of the K-rich zones flanking the cracks by in-diffusion of K from the crack surfaces into the cation-exchanged feldspar during annealing at 550 °C in contact with the salt may thus have produced secondary cracks approximately parallel to the crack walls that had previously been induced during primary cation exchange. These secondary cracks may explain the second population of INAS inferred from the $n_s(T)$ curve of sample FS08-64o. The mechanisms underlying chemically induced fracturing are addressed in the next section.

3.3 Chemically induced fracturing in alkali feldspar

In general, the lattice parameters of a crystalline solid solution depend on its chemical composition, and mechanical stress may be induced in a single crystal, when it undergoes nonuniform compositional change (Larche and Cahn, 1982). If in a brittle crystal the stress level exceeds a critical value, it will undergo fracturing. The rationale underlying the exploitation of this phenomenon for generating cracks in alkali feldspar is based on the notion that alkali feldspar is a brittle mineral, and its lattice parameters show a strongly

anisotropic compositional dependence. Generally, the crystal structure of alkali feldspar contracts with a compositional shift from K-rich towards more Na-rich compositions, where the effect is largest in the direction of the crystallographic a axis and less pronounced parallel to the crystallographic b and c axes (Kroll et al., 1986; Angel et al., 2012). It is known from earlier work (Petrishcheva et al., 2014; Petrovic, 1972; Schäffer et al., 2014b) that the rate of Na–K exchange between alkali feldspar and an NaCl–KCl salt melt is controlled by the interdiffusion of Na and K in the alkali feldspar. The diffusion of Na into a single crystal of K-rich alkali feldspar thus produces a Na-rich surface layer, the thickness of which increases with time.

According to the compositional dependence of the lattice parameters of alkali feldspar, a compositional eigenstrain is induced within the Na-rich surface layer, which is characterized by contraction primarily sub-parallel to the crystallographic a direction. The Na-rich surface layer and the unaltered alkali feldspar beyond the chemically altered surface layer pertain to a single solid and are mechanically coupled, and, as long as the chemically altered surface layer is thin compared to the size of the unaltered core region of the grain, the chemically induced lattice contraction in the Na-rich surface layer is largely compensated by elastic distension to keep the lattice dimensions compatible across the compositional transition zone separating the unaltered core from the chemically altered surface layer. This leads to a tensile stress state in the Na-rich surface layer, where the maximum tensile stress component is approximately parallel to the direction of maximum lattice contraction, which is approximately parallel to the crystallographic a axis. If this tensile stress exceeds about 300 MPa, the surface layer yields by fracturing (Neusser et al., 2012; Scheidl et al., 2014), producing a

set of parallel cracks oriented approximately perpendicular to the *a* axis, which is close to the orientation of the Murchison plane and of the (100) lattice plane. The cracks show quite uniform spacing, which depends on the extent of the applied compositional shift (Scheidl et al., 2014). As soon as the cracks are formed, they are infiltrated by the salt melt, and the crack walls serve as new surfaces, where cation exchange takes place. This leads to a situation, where the cracks propagate independently, irrespective of the stress state at the original crystal surface. Eventually, this may lead to complete disintegration of the original grain into smaller fragments (Petrishcheva et al., 2019; Predan et al., 2020). As the fragments are in part bounded by the crack surfaces and as these are sub-parallel to the (100) lattice plane, these particles have a high proportion of (100) surface exposed. In addition, larger particles have cracks with orientations close to (100). Although shifting of K-rich alkali feldspar towards more Na-rich compositions by cation exchange is an efficient route for producing (100) crystal surfaces in experiment, this mechanism very likely is not relevant in nature. Nevertheless, similarly oriented parting planes following the Murchison plane may be generated by eigenstrain effects during perthite formation and possibly by subsequent hydrothermal alteration. This mechanism is addressed in the next section.

3.4 Formation of feldspar surfaces sub-parallel to (100) by exsolution and their potential contribution to the enhancement of the IN efficacy

Above about 600 °C, depending on pressure and Ca content, alkali feldspar shows complete miscibility. Towards lower temperature, which is a homogeneous alkali feldspar solid solution of intermediate composition is thermodynamically metastable or unstable (Brown and Parsons, 1984). If alkali feldspar of intermediate composition is cooled into the two-phase region of its phase diagram, it exsolves typically forming a lamellar intergrowth of more Na-rich and more K-rich domains giving rise to perthite microstructure (Brown and Parsons, 1984). The lamellar intergrowth is coherent, at least during the early stages of exsolution, and, due to the compositional dependence of the lattice parameters of alkali feldspar (Angel et al., 2012; Kroll et al., 1986), the compositionally distinct lamellae exhibit considerable lattice misfit. In coherent intergrowth this lattice misfit is compensated by elastic deformation of the lamellae. The strong anisotropy of the chemically induced eigenstrain exerts a first-order control on the orientation of the exsolution lamellae. Typically, the exsolution lamellae are oriented parallel to the Murchison plane, which ensures the minimum possible crystallographic misfit between the Na-rich and the K-rich lamellae and is oriented approximately perpendicular to the direction of maximum compositionally induced eigenstrain (Laves, 1952; Robin, 1974; Williame and Brown, 1974). Orientation of the exsolution lamellae parallel to the Murchison plane ensures that the elastic strain energy associated with coherent inter-

growth of Na-rich and K-rich lamellae is minimized. Nevertheless, coherency stress is induced during exsolution. In natural exsolved alkali feldspars the lattice misfit at the lamella interfaces is partially accommodated by edge dislocations lying in the interface planes (Lee and Parsons, 1995; Fitz Gerald et al., 2006; Abart et al., 2009). Around these edge dislocations the feldspar is strained and prone to dissolution in the course of sub-solidus hydrothermal alteration and weathering (Parsons et al., 2005; Lee et al., 1995). Parting planes following the Murchison plane are known from *murchisonite*, a variety of perthite characterized by pseudo cleavage along these non-rational planes (Bollmann and Nissen, 1968). At any rate, alignment of edge dislocations at the lamella interfaces leads to mechanical weakening of these interfaces and fosters disintegration of the feldspar by fracturing along the lamella interfaces. The lamellar interfaces and hence the related parting planes are sub-parallel to the (100) plane. Disintegration of exsolved perthitic alkali feldspar due to mechanical stress thus tends to occur along the lamella interfaces and thus very likely exposes patches of (100) surfaces on the disintegrated feldspar particles (Parsons et al., 2005). In addition, the line defects along the semi-coherent lamellar boundaries may develop into corrosion channels during hydrothermal alteration and weathering (Parsons, 1978; Lee et al., 1995). Such corrosion channels may become sufficiently large to serve as nucleation sites for ice crystals on patches of (100) surfaces exposed on the walls of such corrosion channels. The fact that deposition ice nucleation on feldspar samples was often observed to be associated with surface defects (Kiselev et al., 2017; Pach and Verdaguer, 2019) suggests that the ice-active sites must be exposed to liquid water which is likely to form inside the cracks due to capillary condensation (Kanji et al., 2017; Koop, 2017; Marcolli, 2014; David et al., 2019). A direct observation of ice nucleation associated with surface defects in perthitic feldspar was recently published by Holden et al. (2019). Finally, the elastic strain energy that is stored in coherent lamellar intergrowth in exsolved alkali feldspar increases its Gibbs energy and makes these minerals prone to fluid-mediated mineral replacement (Brown and Parsons, 1993; Parsons and Lee, 2008). Fluid-mediated mineral replacement of exsolved alkali feldspar produces nano-porosity (Putnis, 2002; Walker et al., 1995; Worden et al., 1990), which is concentrated along lamellar interfaces (Abart et al., 2009; Tajčmanová et al., 2012) and likely exposes patches of (100) crystal surfaces, which may serve as ice nucleation sites. This scenario probably applies to the natural Pakistan feldspar (sample FS06-010), which has porosity that was probably generated during hydrothermal processes or deuteric alteration.

4 Conclusions

One of the possible explanations suggested for the repeatedly observed ice nucleation in the pores and cracks on the surface of alkali feldspars is the presence of small patches of crystal surface with (100) orientation that are exposed in the cracks due to natural fracturing or hydrothermal/deuteric alteration of alkali feldspar. Up to now, experimental evidence corroborating this hypothesis was missing. Here, we test this hypothesis experimentally and propose a mechanism explaining why such (100) surfaces are preferentially found in cracks in alkali feldspar. To this end, K-rich gem-quality alkali feldspar was shifted towards more Na-rich compositions by cation exchange with molten NaCl–KCl salt at 850 °C and ambient pressure to exploit the associated anisotropic chemically induced contraction of the crystal structure. Through this treatment, a system of parallel cracks with orientations approximately parallel to the Murchison plane, an irrational plane in alkali feldspar along which the lattice misfit between more Na-rich and more K-rich alkali feldspars is minimized, was generated. The Murchison plane is oriented close to (100), and the somewhat uneven crack surfaces likely contain patches of (100) crystal surfaces. A substantial enhancement of the overall INAS density in the cation-exchanged samples as compared to the untreated reference material corroborates the high IN activity of the chemically induced cracks, which we relate to the presence of patches of (100) crystal surfaces on the crack surfaces. Annealing of the cation-exchanged alkali feldspars at 550 °C in vacuum subsequent to the primary cation exchange lead to an extension of the cracks, which further enhanced the ice-nucleating efficacy of the sample. Annealing of the cation-exchanged feldspar at 550 °C in the presence of the salt leads to the formation of a K-rich surface layer along the crystal surfaces and along the surfaces of the previously induced cracks due to reversed cation exchange at the lower annealing temperature. It is hypothesized that this may have induced secondary surface-parallel cracks which enhanced the IN activity and created new types of ice-nucleating active sites with IN activity at temperatures as high as −3 °C. Our results confirm that chemically induced fracturing in alkali feldspar is a viable mechanism for increasing the INAS density of alkali feldspar. This mechanism is, however, unlikely to play a significant role in the conditioning of natural feldspar, as interaction between alkali feldspar with an inorganic salt melt is unlikely in natural environments. In natural alkali feldspars, parting planes following the Murchison plane may, however, occur due to the mechanical effects associated with exsolution. Separation of initially homogeneous alkali feldspar into lamellae of more Na-rich and a more K-rich alkali feldspar during cooling is a widespread phenomenon in natural alkali feldspar. The chemical eigenstrain associated with exsolution and the resulting lattice mismatch between the two phases are accommodated by elastic strain and/or by the introduction of misfit dislocations at the lamellar boundaries. Both phenomena make lamella interfaces prone to alteration and corrosion during hydrothermal alteration and weathering, which may eventually lead to parting along the Murchison plane. The evolution of a perthite microstructure in alkali feldspar thus fosters the exposure of (100) crystal surfaces and thus enhances the IN activity of exsolved alkali feldspars, a scenario which probably applies to sample FS06-010 investigated in this study. The low IN efficacy of the original sanidine (sample FS08-VS) is explained by the fact that this gem-quality sanidine is homogeneous on the nanometer-scale and is devoid of cracks, inclusions, or perthitic structure. The random milling of a single crystal of this material apparently produces fragments mostly bounded by (001) and (010) cleavage planes. These particles very likely only expose a subordinate fraction of (100)-oriented patches on their surface.

Author contributions. AAK and RA conceived the idea of the study and wrote this article with contributions from all authors. AK and TG conducted the droplet-freezing assay experiment and evaluated the results with contribution from TL and AAK. CS and EP conducted cation exchange experiments and sample preparation. All authors contributed to the discussion of the results.

Review statement. This paper was edited by Ryan Sullivan and reviewed by Thomas F. Whale and one anonymous referee.

References

Abart, R., Petrishcheva, E., Wirth, R., and Rhede, D.: Exsolution by spinodal decomposition II: Perthite formation during slow cooling of anatexites from Ngoronghoro, Tanzania, Am. J. Sci., 309, 450–475, https://doi.org/10.2475/06.2009.02, 2009.

Angel, R., Kolbus, L., and Tribaudino, M.: Tilts and tetrahedra: The origin of the anisotropy of feldspars, Am. Mineral., 97, 765–778, https://doi.org/10.2138/am.2012.4011, 2012.

Atkinson, J. D., Murray, B. J., Woodhouse, M. T., Whale, T. F., Baustian, K. J., Carslaw, K. S., Dobbie, S., O'Sullivan, D., and Malkin, T. L.: The importance of feldspar for ice nucleation by mineral dust in mixed-phase clouds, Nature, 498, 355–358, https://doi.org/10.1038/nature12278, 2013.

Bollmann, W. and Nissen, H.-U.: A study of optimal phase boundaries: the case of exsolved alkali feldspars, Acta Crystallogr. A, 24, 546–557, https://doi.org/10.1107/S0567739468001178, 1968.

Bony, S., Colman, R., Kattsov, V. M., Allan, R. P., Bretherton, C. S., Dufresne, J.-L., Hall, A., Hallegatte, S., Holland, M. M., Ingram, W., Randall, D. A., Soden, B. J., Tselioudis, G., and Webb, M. J.: How well do we understand and evaluate climate change feedback processes?, J. Climate, 19, 3445–3482, https://doi.org/10.1175/JCLI3819.1, 2006.

Boucher, O., Randall, D., Artaxo, P., Bretherton, C., Feingold, G., Forster, P., Kerminen, V.-M., Kondo, Y., Liao, H., Lohmann, U., Rasch, P., Satheesh, S. K., Sherwood, S., Stevens, B., and Zhang, X.-Y.: Clouds and Aerosols, in: Climate Change 2013: The Physical Science Basis. Contribution of Working Group I to the Fifth Assessment Report of the Intergovernmental Panel on Climate Change, edited by: Stocker, T. F., Qin, D., Plattner, G.-K., Tignor, M., Allen, S. K., Boschung, J., Nauels, A., Xia, Y., Bex, V., and Midgley, P. M., Cambridge University Press, Cambridge, 571–658, 2014.

Brown, W. L. and Parsons, I.: Exsolution and coarsening mechanisms and kinetics in an ordered cryptoperthite series, Contrib. Mineral. Petr., 86, 3–18, https://doi.org/10.1007/BF00373706, 1984.

Brown, W. L. and Parsons, I.: Storage and release of elastic strain energy: the driving force for low-temperature reactivity and alteration of alkali feldspar, in: Defects and processes in the solid state: geoscience applications. The Mclaren volume, edited by: Boland, J. and Fitz Gerald, J. D., Elsevier Science Publishers BV, Amsterdam, 267–290, 1993.

Brunauer, S., Emmett, P. H., and Teller, E.: Adsorption of gases in multimolecular layers, J. Am. Chem. Soc., 60, 309–319, https://doi.org/10.1021/ja01269a023, 1938.

Connolly, P. J., Möhler, O., Field, P. R., Saathoff, H., Burgess, R., Choularton, T., and Gallagher, M.: Studies of heterogeneous freezing by three different desert dust samples, Atmos. Chem. Phys., 9, 2805–2824, https://doi.org/10.5194/acp-9-2805-2009, 2009.

David, R. O., Marcolli, C., Fahrni, J., Qiu, Y., Perez Sirkin, Y. A., Molinero, V., Mahrt, F., Brühwiler, D., Lohmann, U., and Kanji, Z. A.: Pore condensation and freezing is responsible for ice formation below water saturation for porous particles, P. Natl. Acad. Sci. USA, 116, 8184–8189, https://doi.org/10.1073/pnas.1813647116, 2019.

Durant, A. J., Shaw, R. A., Rose, W. I., Mi, Y., and Ernst, G. G. J.: Ice nucleation and overseeding of ice in volcanic clouds, J. Geophys. Res.-Atmos., 113, D09206, https://doi.org/10.1029/2007jd009064, 2008.

Durant, A. J., Bonadonna, C., and Horwell, C. J.: Atmospheric and Environmental Impacts of Volcanic Particulates, Elements, 6, 235–240, https://doi.org/10.2113/gselements.6.4.235, 2010.

Fitz Gerald, J. D., Parsons, I., and Cayzer, N.: Nanotunnels and pull-aparts: Defects of exsolution lamellae in alkali feldspars, Am. Mineral., 91, 772–783, https://doi.org/10.2138/am.2006.2029, 2006.

Harrison, A. D., Whale, T. F., Carpenter, M. A., Holden, M. A., Neve, L., O'Sullivan, D., Vergara Temprado, J., and Murray, B. J.: Not all feldspars are equal: a survey of ice nucleating properties across the feldspar group of minerals, Atmos. Chem. Phys., 16, 10927–10940, https://doi.org/10.5194/acp-16-10927-2016, 2016.

Hiranuma, N., Hoffmann, N., Kiselev, A., Dreyer, A., Zhang, K., Kulkarni, G., Koop, T., and Möhler, O.: Influence of surface morphology on the immersion mode ice nucleation efficiency of hematite particles, Atmos. Chem. Phys., 14, 2315–2324, https://doi.org/10.5194/acp-14-2315-2014, 2014.

Hiranuma, N., Augustin-Bauditz, S., Bingemer, H., Budke, C., Curtius, J., Danielczok, A., Diehl, K., Dreischmeier, K., Ebert, M., Frank, F., Hoffmann, N., Kandler, K., Kiselev, A., Koop, T., Leisner, T., Möhler, O., Nillius, B., Peckhaus, A., Rose, D., Weinbruch, S., Wex, H., Boose, Y., DeMott, P. J., Hader, J. D., Hill, T. C. J., Kanji, Z. A., Kulkarni, G., Levin, E. J. T., McCluskey, C. S., Murakami, M., Murray, B. J., Niedermeier, D., Petters, M. D., O'Sullivan, D., Saito, A., Schill, G. P., Tajiri, T., Tolbert, M. A., Welti, A., Whale, T. F., Wright, T. P., and Yamashita, K.: A comprehensive laboratory study on the immersion freezing behavior of illite NX particles: a comparison of 17 ice nucleation measurement techniques, Atmos. Chem. Phys., 15, 2489–2518, https://doi.org/10.5194/acp-15-2489-2015, 2015.

Holden, M. A., Whale, T. F., Tarn, M. D., O'Sullivan, D., Walshaw, R. D., Murray, B. J., Meldrum, F. C., and Christenson, H. K.: High-speed imaging of ice nucleation in water proves the existence of active sites, Sci. Adv., 5, eaav4316, https://doi.org/10.1126/sciadv.aav4316, 2019.

Hoose, C. and Möhler, O.: Heterogeneous ice nucleation on atmospheric aerosols: a review of results from laboratory experiments, Atmos. Chem. Phys., 12, 9817–9854, https://doi.org/10.5194/acp-12-9817-2012, 2012.

Ickes, L., Welti, A., Hoose, C., and Lohmann, U.: Classical nucleation theory of homogeneous freezing of water: thermodynamic and kinetic parameters, Phys. Chem. Chem. Phys., 17, 5514–5537, https://doi.org/10.1039/C4CP04184D, 2015.

Kanji, Z. A., Ladino, L. A., Wex, H., Boose, Y., Burkert-Kohn, M., Cziczo, D. J., and Krämer, M.: Overview of

Ice Nucleating Particles, Meteorol. Monogr., 58, 1.1–1.33, https://doi.org/10.1175/amsmonographs-d-16-0006.1, 2017.

Kiselev, A.: Supplementary data for the manuscript "Effect of chemically induced fracturing on the ice nucleation activity of alkali feldspar" [data set], https://publikationen.bibliothek.kit.edu/1000132261, last access: last access: 2 August 2021.

Kiselev, A., Bachmann, F., Pedevilla, P., Cox, S. J., Michaelides, A., Gerthsen, D., and Leisner, T.: Active sites in heterogeneous ice nucleation – the example of K-rich feldspars, Science, 355, 367–371, https://doi.org/10.1126/science.aai8034, 2017.

Koop, T.: Crystals creeping out of cracks, P. Natl. Acad. Sci., 114, 797–799, https://doi.org/10.1073/pnas.1620084114, 2017.

Kroll, H., Schmiemann, I., and von Coelln, G.: Feldspar solid solutions, Am. Mineral., 71, 1–16, 1986.

Larche, F. C. and Cahn, J. W.: The effect of self-stress on diffusion in solids, Acta Metall. Mater., 30, 1835–1846, 1982.

Laves, F.: Phase Relations of the Alkali Feldspars. II. The Stable and Pseudo-Stable Phase Relations in the Alkali Feldspar System, J. Geol., 60, 549–574, https://doi.org/10.1086/626022, 1952.

Lee, M. R. and Parsons, I.: Microtextural controls of weathering of perthitic alkali feldspars, Geochim. Cosmochim. Ac., 59, 4465–4488, https://doi.org/10.1016/0016-7037(95)00255-X, 1995.

Lee, M. R., Waldron, K. A., and Parsons, I.: Exsolution and alteration microtextures in alkali feldspar phenocrysts from the Shap granite, Mineral. Mag., 59, 63–78, https://doi.org/10.1180/minmag.1995.59.394.06, 1995.

Marcolli, C.: Deposition nucleation viewed as homogeneous or immersion freezing in pores and cavities, Atmos. Chem. Phys., 14, 2071–2104, https://doi.org/10.5194/acp-14-2071-2014, 2014.

McFarquhar, G. M., Yang, P., Macke, A., and Baran, A. J.: A New Parameterization of Single Scattering Solar Radiative Properties for Tropical Anvils Using Observed Ice Crystal Size and Shape Distributions, J. Atmos. Sci., 59, 2458–2478, https://doi.org/10.1175/1520-0469(2002)059<2458:ANPOSS>2.0.CO;2, 2002.

Murray, B. J., O'Sullivan, D., Atkinson, J. D., and Webb, M. E.: Ice nucleation by particles immersed in supercooled cloud droplets, Chem. Soc. Rev., 41, 6519–6554, https://doi.org/10.1039/c2cs35200a, 2012.

Neusser, G., Abart, R., Fischer, F. D., Harlov, D., and Norberg, N.: Experimental Na/K exchange between alkali feldspar and an NaCl–KCl salt melt: chemically induced fracturing and element partitioning, Contrib. Mineral. Petr., 164, 341–358, https://doi.org/10.1007/s00410-012-0741-9, 2012.

Pach, E. and Verdaguer, A.: Pores Dominate Ice Nucleation on Feldspars, J. Phys. Chem. C, 123, 20998–21004, https://doi.org/10.1021/acs.jpcc.9b05845, 2019.

Parsons, I.: Feldspars and fluids in cooling plutons, Mineral. Mag., 42, 1–17, https://doi.org/10.1180/minmag.1978.042.321.01, 1978.

Parsons, I. and Lee, M. R.: Mutual replacement reactions in alkali feldspars I: microtextures and mechanisms, Contrib. Mineral. Petr., 157, 641, https://doi.org/10.1007/s00410-008-0355-4, 2008.

Parsons, I., Thompson, P., Lee, M., and Cayzer, N.: Alkali Feldspar Microtextures as Provenance Indicators in Siliciclastic Rocks and Their Role in Feldspar Dissolution During Transport and Diagenesis, J. Sediment. Res., 75, 921–942, https://doi.org/10.2110/jsr.2005.071, 2005.

Peckhaus, A., Kiselev, A., Hiron, T., Ebert, M., and Leisner, T.: A comparative study of K-rich and Na/Ca-rich feldspar ice-nucleating particles in a nanoliter droplet freezing assay, Atmos. Chem. Phys., 16, 11477–11496, https://doi.org/10.5194/acp-16-11477-2016, 2016.

Petrishcheva, E., Abart, R., Schäffer, A.-K., Habler, G., and Rhede, D.: Sodium-potassium interdiffusion in potassium-rich alkali feldspar I: Full diffusivity tensor at 850 °C, Am. J. Sci., 314, 1284–1299, https://doi.org/10.2475/09.2014.02, 2014.

Petrishcheva, E., Rieder, M., Predan, J., Fischer, F. D., Giester, G., and Abart, R.: Diffusion-controlled crack propagation in alkali feldspar, Phys. Chem. Miner., 46, 15–26, https://doi.org/10.1007/s00269-018-0983-9, 2019.

Petrishcheva, E., Tiede, L., Schweinar, K., Habler, G., Li, C., Gault, B., and Abart, R.: Spinodal decomposition in alkali feldspar studied by atom probe tomography, Phys. Chem. Miner., 47, 30, https://doi.org/10.1007/s00269-020-01097-4, 2020.

Petrovic, R.: Alkali diffusion in alkali feldspars, PhD thesis, Yale University, New Haven, Connecticut, USA, 1972.

Predan, J., Kegl, M., Abart, R., Fischer, F. D., and Rammerstorfer, F. G.: On an alternative approach for simulating chemically induced crack pattern evolutions in a single crystal, Int. J. Solids Struct., 202, 575–586, https://doi.org/10.1016/j.ijsolstr.2020.06.006, 2020.

Putnis, A.: Mineral replacement reactions: from macroscopic observations to microscopic mechanisms, Mineral. Mag., 66, 689–708, https://doi.org/10.1180/0026461026650056, 2002.

Ribbe, P. H.: Feldspar Mineralogy, Rev. Mineral. Geochem., 2, 1–20, 1983.

Robin, P.-Y.: Stress and Strain in Cryptoperthite Lamellae and the Coherent Solvus of Alkali Feldspars, Am. Mineral., 59, 1299–1318, 1974.

Schäffer, A.-K., Jäpel, T., Zaefferer, S., Abart, R., and Rhede, D.: Lattice strain across Na–K interdiffusion fronts in alkali feldspar: an electron back-scatter diffraction study, Phys. Chem. Miner., 41, 795–804, https://doi.org/10.1007/s00269-014-0692-y, 2014a.

Schäffer, A.-K., Petrishcheva, E., Habler, G., Abart, R., Rhede, D., and Giester, G.: Sodium-potassium interdiffusion in potassium-rich alkali feldspar II: Composition- and temperature-dependence obtained from cation exchange experiments, Am. J. Sci., 314, 1300–1318, https://doi.org/10.2475/09.2014.03, 2014b.

Scheidl, K. S., Schaeffer, A. K., Petrishcheva, E., Habler, G., Fischer, F. D., Schreuer, J., and Abart, R.: Chemically induced fracturing in alkali feldspar, Phys. Chem. Miner., 41, 1–16, https://doi.org/10.1007/s00269-013-0617-1, 2014.

Smith, J. V. and Brown, W. L.: Feldspar minerals, 2nd Edn., Springer, Berlin Heidelberg, 1988.

Soni, A. and Patey, G. N.: Simulations of water structure and the possibility of ice nucleation on selected crystal planes of K-feldspar, J. Chem. Phys., 150, 214501, https://doi.org/10.1063/1.5094645, 2019.

Tajčmanová, L., Abart, R., Wirth, R., Habler, G., and Rhede, D.: Intracrystalline microstructures in alkali feldspars from fluid-deficient felsic granulites: a mineral chemical and TEM study, Contributions to Miner. Petrol., 164, 715–729, https://doi.org/10.1007/s00410-012-0772-2, 2012.

Tang, M., Cziczo, D. J., and Grassian, V. H.: Interactions of Water with Mineral Dust Aerosol: Water Adsorption, Hygroscopicity, Cloud Condensation, and Ice Nucleation, Chem. Rev., 116, 4205–4259, https://doi.org/10.1021/acs.chemrev.5b00529, 2016.

Vali, G.: Repeatability and randomness in heterogeneous freezing nucleation, Atmos. Chem. Phys., 8, 5017–5031, https://doi.org/10.5194/acp-8-5017-2008, 2008.

Walker, F. D. L., Lee, M. R., and Parsons, I.: Micropores and micropermeable texture in alkali feldspars: geochemical and geophysical implications, Mineral. Mag., 59, 505–534, https://doi.org/10.1180/minmag.1995.059.396.12, 1995.

Whale, T. F., Holden, M. A., Kulak, A. N., Kim, Y.-Y., Meldrum, F. C., Christenson, H. K., and Murray, B. J.: The role of phase separation and related topography in the exceptional ice-nucleating ability of alkali feldspars, Phys. Chem. Chem. Phys., 19, 31186–31193, https://doi.org/10.1039/C7CP04898J, 2017.

Williame, C. and Brown, W. L.: A coherent elastic model for the determination of the orientation of exsolution boundaries: Application to the feldspars, Acta Crystallogr. A, 30, 316–331, https://doi.org/10.1107/s0567739474010783, 1974.

Worden, R. H., Walker, F. D. L., Parsons, I., and Brown, W. L.: Development of microporosity, diffusion channels and deuteric coarsening in perthitic alkali feldspars, Contrib. Mineral. Petr., 104, 507–515, https://doi.org/10.1007/BF00306660, 1990.

Work, W. J., Horie, K., Hess, M., and Stepto, R. F. T.: Definition of terms related to polymer blends, composites, and multiphase polymeric materials (IUPAC Recommendations 2004), Pure Appl. Chem., 76, 1985, https://doi.org/10.1351/pac200476111985, 2004.

Wright, T. P. and Petters, M. D.: The role of time in heterogeneous freezing nucleation, J. Geophys. Res.-Atmos., 118, 3731–3743, https://doi.org/10.1002/jgrd.50365, 2013.